"Extraordinary" modulation instability in optics and hydrodynamics

Guillaume Vanderhaegen[a,1], Corentin Naveau[a], Pascal Szriftgiser[a], Alexandre Kudlinski[a], Matteo Conforti[a], Arnaud Mussot[a,b], Miguel Onorato[c], Stefano Trillo[d], Amin Chabchoub[e,f], and Nail Akhmediev[g]

[a]University of Lille, CNRS, UMR 8523-PhLAM-Physique des Lasers Atomes et Molécules, F-59000 Lille, France; [b]Institut Universitaire de France, F-75005 Paris, France; [c]Dipartimento di Fisica, Università degli Studi di Torino, 10125 Torino, Italy; [d]Department of Engineering, University of Ferrara, 44122 Ferrara, Italy; [e]Centre for Wind, Waves and Water, School of Civil Engineering, The University of Sydney, Sydney, NSW 2006, Australia; [f]Disaster Prevention Research Institute, Kyoto University, Kyoto 611-0011, Japan; and [g]Department of Theoretical Physics, Research School of Physics, The Australian National University, Canberra, ACT 2600, Australia

The classical theory of modulation instability (MI) attributed to Bespalov–Talanov in optics and Benjamin–Feir for water waves is just a linear approximation of nonlinear effects and has limitations that have been corrected using the exact weakly nonlinear theory of wave propagation. We report results of experiments in both optics and hydrodynamics, which are in excellent agreement with nonlinear theory. These observations clearly demonstrate that MI has a wider band of unstable frequencies than predicted by the linear stability analysis. The range of areas where the nonlinear theory of MI can be applied is actually much larger than considered here.

nonlinear waves | modulation instability | breathers

Well-known Bespalov–Talanov (BT) (1) and Benjamin–Feir (BF) (2, 3) instabilities discovered more than 50 years ago (1966 and 1967, respectively) played a significant role in understanding nonlinear phenomena in optics and hydrodynamics (4–11). The detailed description of these fundamental results can be found in any common book on nonlinear optics (12, 13), ocean waves (14, 15), and more generally, in nonlinear dynamics book literature (16). The theory tells us that a plane wave or a constant-amplitude wave (CW) is unstable relative to small-amplitude perturbations with frequencies within certain deterministic and finite range. These perturbations are unstable and can grow exponentially, thus leading to modulated waves with infinitely high amplitude. Clearly, such growth is unphysical and has to be reconsidered using an approach beyond linear theory. Indeed, the accurate nonlinear theory (17) predicts saturation and the maximal amplitude of periodic waves excited due to modulation instability (MI). This prediction is in accordance with conventional wisdom: "What goes up must come down." In fact, this nonlinear stage of MI predicted not only the exponential growth but the following exponential decay back to the CW (17). The latter was not obvious and required many years before this seemingly simple principle "must come down" was confirmed, first with the observation of growth saturation in water waves (4) and then with the demonstration of the full recursive behavior in optical experiments (18, 19). If translated to the frequency domain, this principle is, essentially, the Fermi–Pasta–Ulam recurrence (20) (also refs. 4, 5, 9–11, and 21).

Despite these achievements, it has been recently demonstrated that not all secrets of MI concealed by the linear approach have been revealed so far (22). The results obtained in ref. 22 demonstrate that the linear theory does not accurately predict the range of unstable frequencies. This fact is, once again, not obvious. Linear stability analysis is an important step in studies of various physical phenomena. One example is the transition from laminar state to turbulent regime in Couette and Poiseuille flows (23). In these cases, experimental data have been in drastic disagreement with the predictions of the linear stability analysis. A few conjectures for this failure have been suggested that included the presence of transverse dimension in the experiment that has not been taken into account in the linear stability analysis. Besides, the Navier–Stokes equations, which describe such flows, are not integrable. Thus, the accurate nonlinear description of the regimes beyond linear state is problematic. An exact nonlinear theory is essential for revealing the full range of frequencies that are unstable due to the modulation. In this sense, our work demonstrates the advantage of dealing with integrable equations that provide solutions beyond the linear dynamics. Exact solutions of the nonlinear Schrödinger equation (NLSE) that describes the nonlinear stage of MI are presently known as Akhmediev breathers (ABs) (24–30). The latter form a family of solutions with a free parameter that is directly related to the whole interval of unstable frequencies in the BT and BF theories. However, even the AB solutions do not cover the whole range of unstable frequencies. The family of ABs is actually a particular case of a more general family of solutions that have been found in ref. 31 and refined recently in ref. 22 (refs. 32–35 also have the application to the normal dispersion regime). This extension expands the range of unstable frequencies predicted in the BT and BF theories. It has important ramifications for theory, experiment, and applications (36–38). It means that periodic perturbations of a plane wave (or CW) can grow in the situations when we would not expect them to do so.

Significance

Modulation instability (MI) is a ubiquitous phenomenon in physics, corresponding to the growth of a weakly modulated continuous wave in a nonlinear medium and leading to the generation of a large-amplitude periodic wave train. In space, it transforms weakly modulated plane waves into spatially periodic patterns. In frequency domain, the MI is the result of energy transfer from a strong single spectral component into sidebands. While linear stability analysis predicts a limited band of unstable frequencies of modulation, recent developments based on a nonlinear theory revealed the existence of MI beyond this limited frequency range. These experimental studies are the first experimental demonstrations of the "extraordinary" MI phenomenon. Achieved both in optics and hydrodynamics, they clearly further highlight the interdisciplinary of this process.

PHYSICS

Presenting simultaneously optical and hydrodynamic experiments confirming this exceptional feature of MI in a single work has far-reaching consequences. Observing the same effect at nearly opposite ends of spatial and timescales of MI in physics is a convincing argument confirming the validity of the finding. It means that similar phenomena at other scales such as MI in plasma (39) or in Bose–Einstein condensate (40) must also be reexamined. In optics, the extension of the range of frequencies leading to MI might have multiple applications for generating frequency combs (41), periodic pulse trains (42), and supercontinuum radiation (43). In hydrodynamics, the findings might result in reconsidering conditions leading to formation of rogue waves in the ocean (44).

Theoretical Background

The family of exact solutions of the NLSE with three free real parameters that explain known and new physical phenomena was presented earlier in ref. 22. Among the new effects covered by this theory is amplification outside the conventional MI band. Here, we provide that part of equations that are necessary for understanding the wider range of unstable MI frequencies and for comparisons with experimental data obtained in the present work that confirm the existence of this interesting effect. We start with the NLSE written in the normalized form:

$$i\psi_z + \frac{1}{2}\psi_{tt} + |\psi|^2\psi = 0, \qquad [1]$$

where ψ is the wave envelope function, z is the longitudinal coordinate, and t is the time in a frame moving with group velocity. This form of the NLSE is a sufficiently accurate model of nonlinear waves in a reasonably wide range of conditions. In optical fibers, these conditions are satisfied at frequency range where anomalous dispersion takes place, while in water waves, this requirement is the condition of deep water. Our experiments are done in these conditions, and good agreement is achieved in each case. Clearly, beyond the ranges of applicability, the accuracy of nonlinear wave description by the NLSE decreases. Then, our theoretical model would require further rectifications. We are interested in doubly periodic waves [e.g., in solutions of Eq. **1** that are periodic both in space and in time (22)]. They comprise the three-parameter family of solutions with a single period along each axis, z and t. This family contains as particular cases other "elementary" solutions and families (22). To be specific, doubly periodic solutions of Eq. **1** can be presented in general form:

$$\psi(t,z) = [Q(t,z) + i\delta(z)]e^{i\phi(z)}, \qquad [2]$$

with the functions $Q(t,z)$, $\delta(z)$, and $\phi(z)$ that can be found by a direct substitution of [2] into [1] (31). There are two forms of such solutions, classified as A- and B-types depending on the parameters of the family. Each type contains MI as the limiting case. However, the limiting case of B-type solutions is the standard MI, while the limiting case of A-type solutions is more general.

This apparently puzzling asymmetry between the two families finds its physical justification in the fact that A-type solutions can be considered as the full nonlinear dressing of solutions of the NLSE obtained in the linear limit (when dispersion dominates over nonlinearity). As discussed in more details in ref. 22, for very high modulation frequencies, the deformation introduced by the nonlinearity is small, and essentially, the modulation experiences, upon evolution, only a periodic phase shift (45). However, when the frequency is reduced to sufficiently small values, the deformation due to the nonlinearity becomes strong, thereby inducing a net amplification of the input sidebands even outside the conventional MI bandwidth. Conversely, B-type solutions start to appear only at frequencies below the conventional band edge of MI, as a result of the

symmetry-breaking nature of the onset of conventional MI (10, 22). Therefore, B-type solutions cannot be responsible for any unconventional MI.

Thus, our point of interest in this work is the A-type solutions, which depend on three arbitrary real parameters α_3, ρ, and η; *Calculation of Theoretical Solutions* has more details. Q, δ, and ϕ are determined as functions of these free parameters (*Analytical Expressions of the Solutions*), which so provide us with the possibility of accurately controlling the wave evolution with periodic initial conditions and particularly, the development of MI.

Instability Outside the Conventional MI Band

The equations presented in *Methods* provide exact wave dynamics with two frequencies. Thus, the MI that is periodic along the t axis is a particular case of these solutions. Indeed, there is a range of parameters ρ and η when the solution represents the growth of a periodic perturbation on top of a continuous wave. This happens when $0 < \rho < 1$ and $\eta \to 0$. This range corresponds to exact conditions of MI with the exponential growth of periodic perturbation with a frequency defined by ρ. On the other hand, for parameters ρ and η beyond this range, the evolution has all features of MI, but the growth of the perturbation takes a different form.

This more general evolution is periodic in z. The solution is closest to the continuous wave when the evolution variable $z = \pm \mathcal{Z}/4$. Starting from one of these values of z leads to the growth of modulations on the background CW. One example is given in Fig. 1*A* that shows wave intensity profiles at $z = -\mathcal{Z}/4$ when the modulation is small (red curve) and at $z = 0$ when the modulation is maximal (blue curve). Pulses within this periodic pulse train are maximally compressed. The wave intensity profile returns back to the initial condition at $z = +\mathcal{Z}/4$.

The amplification of the periodic component of the solution calculated numerically from the exact solution is shown in Fig. 1*B*. Here, the frequency range [0, 2] is the standard band of MI. Amplification within this range is not surprising. However, the amplification is not zero when the frequency $\omega > 2$. The amplification here might seem smaller than within the band [0,2]. However, the amplitudes of the pulse trains reached due to the growth are of the same order of magnitude as within the band. Thus, the effect is easily measurable in experiments. Moreover, the frequency range shown in Fig. 1*B* is nearly 1.5 times the conventional MI bandwidth $\omega \in [0, 2]$. In reality, it is much wider than in this figure. Even from this point of view, the effect is easily observable. As can be seen from Fig. 1*B*, the value of amplification depends on the parameter η. For larger
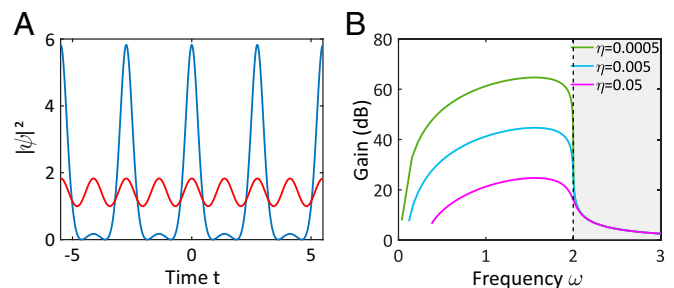

Fig. 1. (*A*) Transformation of a periodic perturbation on top of the CW (red curve) into a train of pulses (blue curve). Parameters of the solution here are $\rho = 0$, $\eta = 1$, and $\alpha_3 = 1$. Modulation frequency $\omega = 2.287 > 2$ is outside of the instability band. (*B*) Amplification of periodic component of the solution vs. frequency. Frequency ω depends on the parameter ρ that changes in the interval $[-3, 1]$. Gray area beyond dashed black line marks the frequency range $\omega > 2$, located outside the conventional MI gain band ($\omega \leq 2$).
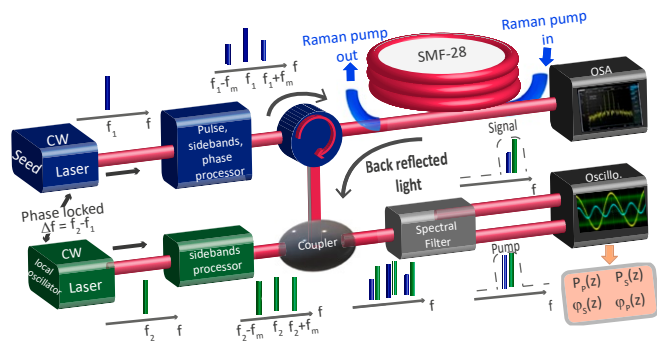
Vanderhaegen et al.
"Extraordinary" modulation instability in optics
and hydrodynamics

Fig. 2. Experimental setup: $f_{1,2}$ are the frequencies of the main laser and the local oscillator laser, respectively. Here, f_m is the input modulation frequency (pump frequency at f_1, input sideband frequencies at $f_1 \pm f_m$). The backscattered signal from the single-mode fiber (Corning SMF-28) goes through a circulator to be analyzed via heterodyning (beating with the local oscillator) and then filtered (wave shaper) to isolate the power and phase evolutions of the pump and the first-order sideband pair in the MI spectral comb. OSA, optical spectrum analyzer; Oscillo., oscilloscope.

values of η, the amplification within the standard MI band is smaller. However, the amplification outside of this band does not depend on η. Thus, at larger values of η, the MI effect is nearly the same order of magnitude within and outside of the standard band.

Another remarkable feature of the MI visible in Fig. 1*A* is the period of the pulse train, which is twice the period of the initial modulation. Every second maxima of the periodic perturbation grows while the juxtaposing maxima decay. This feature adds flexibility to potential applications of the effect. The red curve in Fig. 1*A* and analogous curves calculated for other values of parameters have been used as initial conditions in the optical and water wave experiments as well as in numerical simulations presented below.

Optical Experiments

For optical experiment, we used a setup similar to the one used in refs. 10 and 46 and devoted to investigating nonlinear stage of MI within its conventional bandwidth. Its schematic is shown in Fig. 2.

The input in the form of continuous wave with periodic perturbation is created by CW laser 1. The intensity and the phase of the pump and the sidebands are precisely controlled. The resulting three-wave input is injected into an $L = 18.28$-km-long single-mode fiber (Corning SMF-28 with group velocity dispersion $\beta_2 = -21 \times 10^{-27}$ s^{2}m^{-1}, nonlinear coefficient $\gamma = 1.3 \times 10^{-3}$ W^{-1}m^{-1}). The loss is actively compensated by using
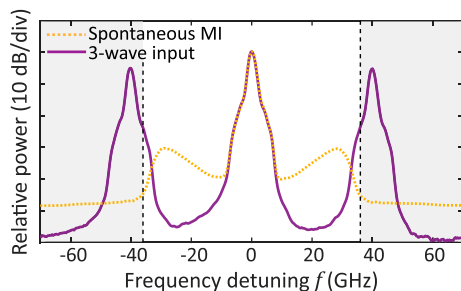

Fig. 3. Experimental three-wave input spectrum (purple solid line) compared with the spontaneous MI spectrum (yellow dotted line). The two gray areas beyond dashed black lines mark the range of frequencies $f > f_C$, located outside of the conventional MI gain band ($f \le f_C$). On the power axis, each division (div) corresponds to a 10 dB variation.

a counterpropagating Raman pump emulating an almost fully transparent optical fiber (10). Power and phase distributions of the pump and the first-order sideband (signal) are obtained using a multiheterodyning technique between the backscattered signal and the local oscillator (10).

The MI cutoff frequency is $f_C = 1/(\pi\sqrt{|\beta_2| L_{NL}})$, with $L_{NL} = (\gamma P_P)^{-1}$ (*Optical Normalization*). The pump power P_P in experiments is set to 180 mW, leading to a cutoff frequency of the conventional MI gain band at $f_C = 33.6$ GHz. In all our experiments, the modulation frequency f_m is located outside the MI gain band (i.e., $f_m > f_C$). The intensity of the sidebands is set at 5.3 dB below the pump power. The experimental spectra of the three-wave input and the spectrum of spontaneous MI (i.e., conventional MI gain band profile) are plotted in Fig. 3. The initial relative phase between the pump and the signal is $-\frac{\pi}{2}$ in order to excite the A-type waves.

Experimental data for $f_m = 40$ GHz and analytical solution for the same set of parameters are shown in Fig. 4.

Fig. 4*A* displays the experimental power evolution of the pump (blue) and the signal (red). The corresponding theoretical prediction is shown by dashed curves. As expected, first we observe amplification of the signal and depletion of the pump. The process reverses at around 2.5 km when the maximum depletion
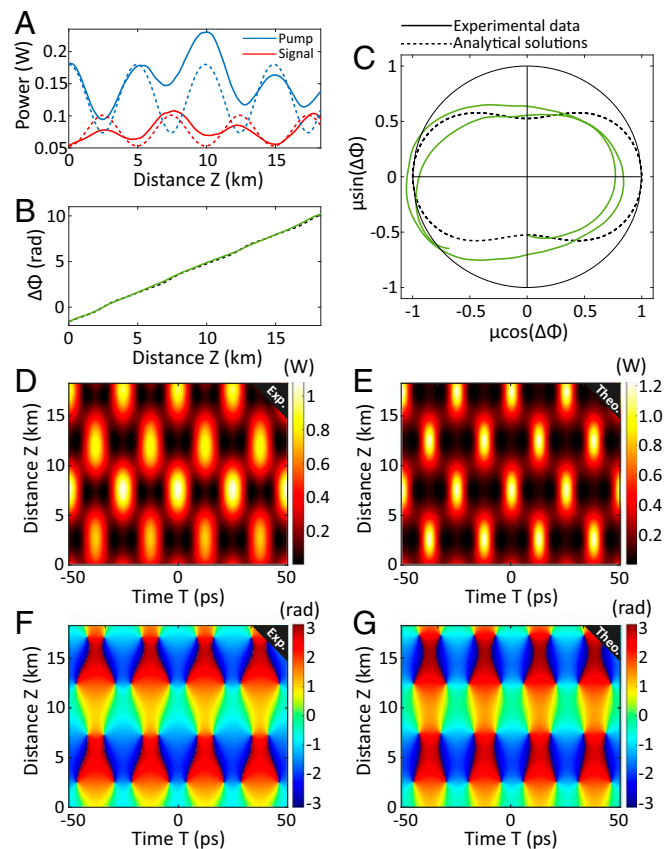

Fig. 4. Three waves evolution along the fiber when the sideband detuning $f_m = 40$ GHz ($\omega_m = 2.3809$) is outside the conventional MI band. (*A*) Evolution of the pump power (blue curves) and signal power (red curves). The solid curves in *A*–*C* correspond to the experimental data, while dashed curves are theoretical. (*B*) Relative phase vs. distance. (*C*) The phase-plane representation of the evolution. (*D* and *E*) Spatiotemporal false-color plots of the power profile. (*F* and *G*) The phase profiles. *D* and *F* show the experimental data, while *E* and *G* are theoretical. The following parameters have been used to prepare the initial conditions in the experiment and to plot the analytical solution: $\eta = 1.2420$, $\rho = 0.0317$, and $\alpha_3 = 1.0$.

Vanderhaegen et al.
"Extraordinary" modulation instability in optics
and hydrodynamics

PNAS | 3 of 7
https://doi.org/10.1073/pnas.2019348118

of the pump is reached. The signal in experiment is amplified by 1.7 dB between its initial value in $Z = 0$ and its first maximum (2.8-dB gain for the corresponding analytical solution). The gain outside the conventional MI bandwidth is lower than the theoretical one shown in Fig. 1B as the values of η in experiments are higher (for $\omega = \omega_m$ and $\eta = 0.05$, the theoretical gain is 5.2 dB).

The first recurrence to the initial power profile occurs at 5 km, and then, successive cycles of growth and decay are repeated. Overall, more than three periods of such oscillatory evolution can be seen in Fig. 4A. Deviation from perfect periodic dynamics is due to an imperfect compensation of loss by the active compensation system. The consequence of this inaccuracy is overamplification of the signal around the 10-km mark. Fig. 4B shows the nearly linear evolution of the pump-signal relative phase ($\Delta\Phi$) over the fiber length. The experimental curve fits the theory almost perfectly. Importantly, the initial phase is recovered after two cycles of power evolution (around $Z = 10$ km), whereas successive maximum amplification stages turn out to be mutually out of phase (sidebands shifted by π), which is a unique feature of A-type solutions (22).

It is also very convenient to illustrate the dynamics of the process in the phase space $[\mu\cos(\Delta\Phi), \mu\sin(\Delta\Phi)]$ where μ is the signal power normalized to its maximum value. Such trajectories are shown in Fig. 4C. The theoretical curve shown by the dashed line is strictly periodic and corresponds to the A-type solution. The quantitative agreement is also pretty good if we focus on the locations of the curve maxima. Fig. 4C also gives a pictorial view of the fact that the sidebands amplification is connected to the nonlinear deformation of the orbit with respect to circular orbits. The net gain indeed arises, in the figure-of-eight–shaped orbit, from the ratio of the signal at the maximum elongation (horizontal axis, $\Delta\Phi = 0, \pi$) and at the maximum orbital squeezing (input, $\Delta\Phi = -\pi/2$).

Fig. 4 D and F shows the spatiotemporal evolutions of the power (Fig. 4D) and phase (Fig. 4F) of the electric field calculated from the inverse Fourier transform of the three main spectral components (Fig. 4 A–C). We used a procedure similar to that in ref. 47. Characteristic chessboard-like patterns are obtained, which is a clear signature of A-type solutions. The
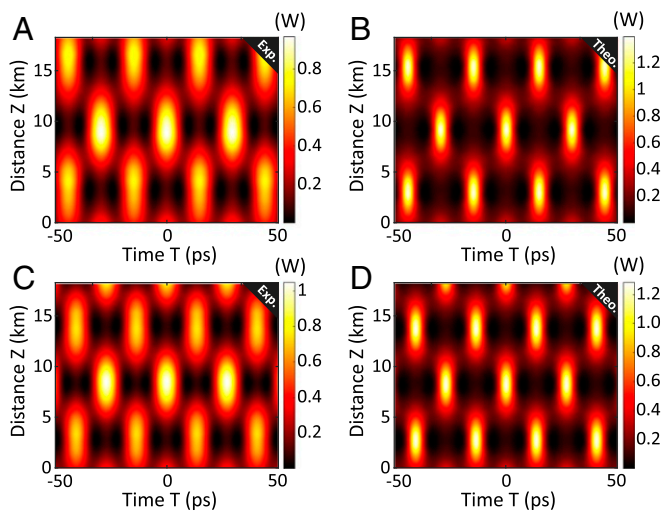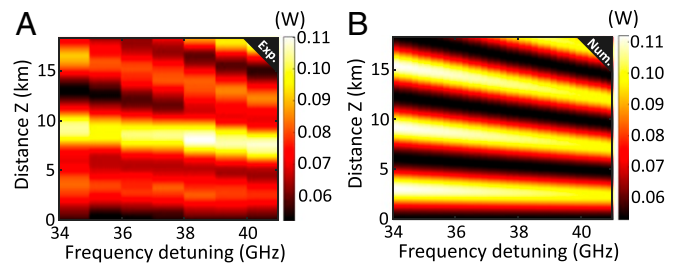

Fig. 6. Two-dimensional plot of the signal power as a function of distance Z (vertical axis) and pump-signal frequency shift (horizontal axis). (*A*) Experiment and (*B*) numerics.

agreement with the analytical solution (Fig. 4 E and G) is very good. We notice, once again, that the input phase is recovered after two grow–decay cycles of power evolution, whereas successive maximal amplification profiles are shifted by half of the transverse period.

Fig. 5 shows two additional spatiotemporal evolutions of the signal power from experimental measurements (Fig. 5 A and C) and from analytics (Fig. 5 B and D). The two signal frequency shifts ($f_m = 34$ and 37 GHz) are still outside of the MI band but located closer to the cutoff frequency. Again, the chessboard-like pattern of these plots confirms the A-type nature of these solutions. We can also notice that when approaching the cutoff frequency, the spatial periods (along z) increase, as can be seen from Figs. 4D and 5 A and C. Importantly, maximal wave amplitudes reached at the points of maximal compression are of the same order of magnitude for all cases shown in these figures.

As mentioned, the spatial (longitudinal) period depends on the shift between the modulation and the pump frequencies. When the modulation frequency is outside of the MI band, this period decreases with the modulation frequency moving away from the pump. Experimental verification of this behavior is shown in Fig. 6A. Fig. 6B shows the corresponding theoretical plot. While the frequency shift increases from 34 to 41 GHz, the number of longitudinal periods along the same distance ≈ 18 km changes from 3 to 3.8. This means that each longitudinal period decreases from ≈ 6 to ≈ 4.73 km. Agreement between the experimental data and the theory is also good as the two plots in Fig. 6 demonstrate. Thus, our optical experiments confirm, clearly, the fact of existence of MI outside of the conventional instability band. The measurements are in good agreement with the theoretical predictions based on the exact solutions of the NLSE.

Water Wave Experiments

The hydrodynamic experiments have been performed in a unidirectional wave tank installed at the University of Sydney and shown in Fig. 7.

Its dimensions are $1 \times 1 \times 30$ m. The tank was filled with fresh water to the height of 0.7 m in order to satisfy the deep water conditions for waves generated at the peak frequencies between 1.5 and 2.0 Hz. The piston wave maker with oscillation frequency range of $0.4 < f < 2$ Hz was installed at the right end of the tank. A wave-absorbing beach is located at the opposite end to eliminate any influence from reflected waves. The piston is activated by an electric actuator, controlled by a preprocessed signal, which allows the seeding of a modulated surface elevation profile, according to mathematical expressions given above.

Eight wave gauges with a sampling rate of 32 Hz each are placed along the tank to collect the water wave elevation data. Due to repeatability of experiments, all eight wave gauges have been repositioned five times along the facility to ensure high resolution of the data acquisition both in time and in space. The

Fig. 5. Spatiotemporal power evolution for two other values of the pump-signal frequency shift. (*A* and *B*) $f_m = 34$ GHz ($\omega_m = 2.0238$); (*C* and *D*) $f_m = 37$ GHz ($\omega_m = 2.2023$). (*A* and *C*) Experimental data. (*B* and *D*) Analytical solution. The following parameters have been used to prepare the initial conditions in the experiment and to plot the analytical solution: (*A* and *B*) $\eta = 1.0385$, $\rho = 0.4275$, $\alpha_3 = 1.0$; and (*C* and *D*) $\eta = 1.1407$, $\rho = 0.2374$, $\alpha_3 = 1.0$.
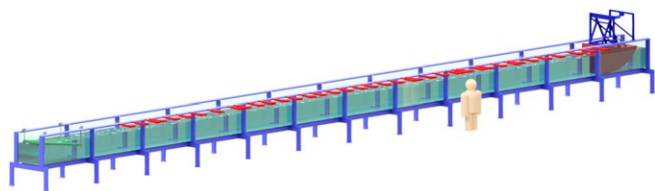
Fig. 7. Sketch of the $L = 30$-m-long water tank at the University of Sydney. In red, the locations of the gauges are shown.

gauges' locations measured from the mean position of piston in these experiments are represented in red in Fig. 7. This gave us sufficient resolution in z for plotting the experimental patterns, as shown below. The wave envelopes have been computed using the Hilbert transform, while the spectral data have been calculated using the fast Fourier transform of the water surface elevation data.

Although the water wave envelope obeys the same dimensionless focusing NLSE as the normalized optical field in optical fiber, the spatial and timescales turn out to be extremely different. We start from dimensional deep water time NLSE (15) characterized by the second-order dispersion coefficient $\beta_2 = -2/g$ ($g = 9.81$ m/s^2 is the gravitational acceleration) and the nonlinear coefficient $\gamma = -\kappa^3$ ($\gamma\beta_2 > 0$, focusing regime), where κ is the wave number of the carrier, with the carrier frequency fixed through the dispersion relation $\omega = \sqrt{g\kappa}$.

Operating with the scaling in Eq. **8** (*Water Wave Normalization* has more details), we obtained the theoretical spatiotemporal patterns shown in Figs. 8B, 9B, and 10B, which we compare with experimental data (Figs. 8A, 9A, and 10A). The choice of the parameters of the NLSE solution used for generating these patterns is given in the figures. In our water waves experiment, typically, $L_{NL} \approx 10$ m and $T_s \approx 1.4$ s compared with $L_{NL} \approx 4$ km and $T_s \approx 10$ ps of the optical experiment. Accordingly, also the MI cutoff frequency, which reads, in this case, $f_C = \frac{1}{\pi}\sqrt{\frac{g\kappa^3 a^2}{2}}$, turns out to be several orders of magnitude lower than the one in optics. For instance, with $\kappa = 10$ m^{-1} and $a = 0.01$ m (case of Fig. 8), we obtain $f_C = 0.22$ Hz. The envelope evolution as predicted by theory takes into account the second-order Stokes correction to the water surface elevation (36).

These spatiotemporal patterns are very similar to those obtained in optical experiments. Remarkably, our maxima (two periods) have been achieved within the length of the tank as can be seen from Fig. 8. The resulting chessboard
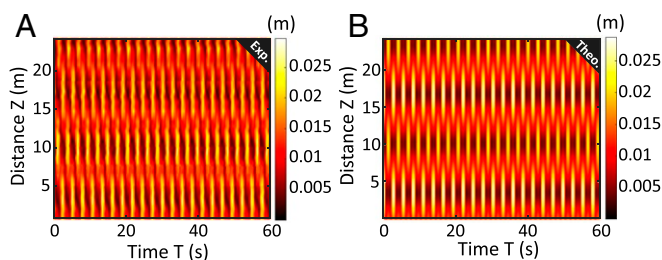

Fig. 9. (*A* and *C*) Experimental and (*B* and *D*) theoretical plots of spatiotemporal wave evolution that start with MI. The values of parameters in the NLSE solution used to prepare the initial conditions in the experiment are (*A* and *B*) $\eta = 1.03$, $\rho = 0.355$, $\alpha_3 = 1.0$; and (*C* and *D*) $\eta = 1.0$, $\rho = 2.0$, $\alpha_3 = 1.0$. Wave amplitude $a = 0.01$ m in each case. The wave numbers of the carrier are (*A*) $\kappa = 10$ m^{-1} and (*C*) $\kappa = 8$ m^{-1}. The corresponding wave steepness $\varepsilon = 0.1$ with cutoff frequency $f_C = 0.22$ Hz in *A* and $a\kappa = 0.08$ with cutoff frequency $f_C = 0.15$ Hz in *C*. The modulation frequency is $f_m = 0.25$ Hz in *A* and $f_m = 0.16$ Hz in *C*.

structure of this pattern corresponding to the A-type doubly periodic wave is also clearly seen. Three recurrences to a nearly CW are clearly visible despite unavoidable dissipation elements, always present when performing laboratory experiments. Note that for the given carrier wave parameters, it would not be possible to observe more than one cycle of MI growth-decay or AB within the given effective propagation distance of 25 m.

In order to reaffirm the observation, two more examples of the spatiotemporal pattern are shown in Fig. 9. These plots contain less than one period of evolution that includes one full recurrence to initial conditions at around the 15-m mark in Fig. 9A and around the 19-m mark in Fig. 9C. In each case, the carrier steepness ε has been adjusted to be just below the threshold of wave breaking. The latter happens due to the excessive wave amplitude amplification.

One essential difference of experimental patterns in Figs. 8A and 9A from the optical ones is slightly tilted vertical stripes. The reason is the asymmetry of the water wave profiles, which is the

Fig. 8. (*A*) Experimental and (*B*) theoretical plots of spatiotemporal wave evolution that start with extraordinary MI. The values of parameters in the NLSE solution used to prepare the initial conditions in the experiment are $\eta = 1.9$, $\rho = -0.9$, and $\alpha_3 = 1.0$. Wave amplitude $a = 0.01$ m, the carrier wave number $\kappa = 10$ m^{-1}, the corresponding wave steepness $\varepsilon = 0.1$, and the modulation frequency $f_m = 0.37$ Hz is well above the cutoff $f_C = 0.22$ Hz.

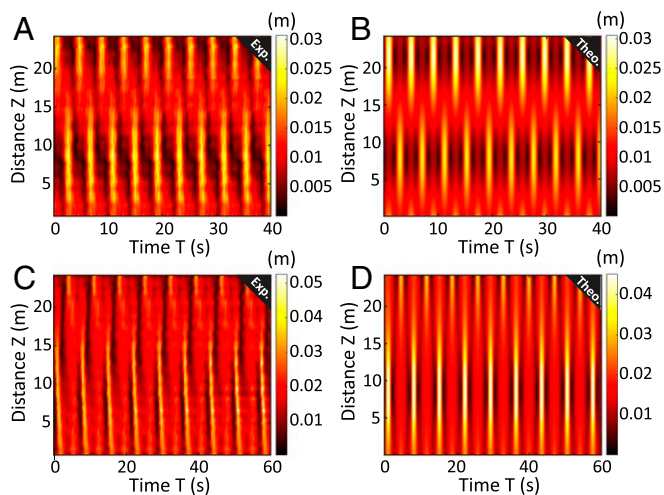**Fig. 10.** (*A*) Experimental and (*B*) theoretical plots of spatiotemporal wave evolution that start with MI. The values of parameters in the NLSE solution used to prepare the initial conditions in the experiment are $\eta = 1.9$, $\rho = 2.9$, and $\alpha_3 = 1.0$. Wave amplitude $a = 0.01$ m. The wave number of the carrier in *A* is $\kappa = 8$ m^{-1}; consequently, the wave steepness $\varepsilon = 0.08$. The modulation frequency here $f_m = 0.2$ Hz is once again above the cutoff frequency $f_C = 0.15$ Hz. MI develops, but wave breaking prevents the recurrence back to initial conditions.

Vanderhaegen et al.
"Extraordinary" modulation instability in optics
and hydrodynamics

PHYSICS

result of significant breather amplification of a factor of three and above. The consequence is the nonlinear Stokes contributions that are always present in water waves at these scales (48, 49). Despite these deviations, the patterns in Figs. 8*A* and 9*A* clearly confirm the presence of the MI and its nonlinear evolution beyond the standard unstable frequencies of MI in the BF theory.

Generally, when increasing the amplification factor of the breather, the steepness has to be decreased in order to avoid wave breaking. The latter violates the condition of the flow to be irrotational and thus, prohibits applicability of the Euler equations and subsequently, the validity of the NLSE (14). Indeed, when this threshold of wave breaking is exceeded, spilling as well as recurrent breaking occurs, and the pattern changes significantly and does not follow the theoretical NLSE predictions. One example is shown in Fig. 10.

Here, the value of the breather parameter ρ is increased in comparison with the previous cases. MI still develops, but there is no obvious recurrence back to initial conditions as can be seen from Fig. 10*A*.

Conclusions and Discussion

In conclusion, we have experimentally confirmed that MI is a more complex phenomenon than the one predicted by the simplified linear stability analysis. The most striking difference that the more accurate nonlinear analysis using exact breather framework reveals is the fact that periodically perturbed continuous waves develop the growth of perturbation not only within the standard MI band described by the BF and BT theories but also outside of it. To be more accurate, the frequency range of unstable growth of the perturbation extends beyond the standard MI threshold.

Another dramatic difference from the standard theory can be seen when observing the nonlinear stage of MI. The subsequent evolution beyond the initial growth creates a specific chessboard-like periodic spatiotemporal pattern of wave propagation. Temporal maxima of the generated pulse trains change position every half period of spatial evolution. The effect tightly related to this phenomenon is the fact that the frequency of the pulse train at the point of maximum compression is half of the frequency of initial modulation. Such phenomenon may find applications in frequency comb devices facilitating the atomic clock synchronization when the frequencies differ by an octave (50).

Having these unusual features revealed in nonlinear analysis, we can call the effect "extended" or "extraordinary" MI. Importantly, we were able to track and confirm this extraordinary MI in two different physical media, namely in optics and in hydrodynamics, proving the interdisciplinary significance of the extended MI. In fact, these are the two areas of physics where the wavelength differs by four orders of magnitude and the modulation frequencies by ten orders of magnitude. This twofold confirmation of the effect shows that it is ubiquitous and does not depend on the scale of the physical system that we operate with. The effects should be also observable in other areas of physics such as astrophysics (51), plasma (52, 53), metamaterials (54), and in Bose–Einstein condensate (55, 56). We envisage that the phenomenon can be useful in applications such as generation of optical frequency combs and pulse trains with prescribed parameters: periods, amplitudes, and duty cycles. Moreover, we anticipate modeling approaches for extreme events in nonlinear dispersive media. Here, we have chosen the NLSE solution that can be considered as the simplest among the variety of more complex wave fields. As such, our work could be the start of a direction in the research of instabilities at the transition stage between the linear and nonlinear regimes of wave dynamics.

Methods

Analytical Expressions of the Solutions. The three functions in [**2**] are defined as follows. Namely, for the function $\delta(z)$, we have the following expression:

$$\delta(z) = \sqrt{\frac{\alpha_3}{2}(1-\nu)}\sqrt{\frac{1+dn(\mu z, k)}{1+\nu cn(\mu z, k)}}sn(\mu z/2, k), \qquad [3]$$

where $m = k^2 = \frac{1}{2}\left(1 - \frac{\eta^2 + \rho(\rho-\alpha_3)}{AB}\right)$, $A^2 = (\alpha_3 - \rho)^2 + \eta^2$, $B^2 = \rho^2 + \eta^2$, $\nu = \frac{A-B}{A+B}$, and $\mu = 4\sqrt{AB}$. The function δ varies within the interval $0 < \delta^2 < \alpha_3$.

The phase $\phi(z)$ is given by

$$\phi(z) = \left(2\rho + \frac{\alpha_3}{\nu}\right)z - \frac{\alpha_3}{\nu\mu}\left[\Pi(am(\mu z, k), n, k) - \right.$$
$$\left. -\nu\sigma \tan^{-1}\left(\frac{sd(\mu z, k)}{\sigma}\right)\right], \qquad [4]$$

where $n = \frac{\nu^2}{\nu^2 - 1}$, $\sigma = \sqrt{\frac{1-\nu^2}{k^2 + (1-k^2)\nu^2}}$, and $sd(\mu z, k) = \frac{sn(\mu z, k)}{dn(\mu z, k)}$, $\Pi(am(\mu z, k), n, k)$ is the incomplete elliptic integral of the third kind with the argument $am(u, k)$ being the amplitude function.

In contrast to δ and ϕ, the function Q depends on two variables t and z. It is given by

$$Q(t, z) = sb - c_+ \frac{r + cn(pt, k_q)}{1 + rcn(pt, k_q)}, \qquad [5]$$

where $s(z) = \text{sign}[cn(\mu z/2, k)]$, $r = \frac{M-N}{M+N}$, $p = \sqrt{MN} = 2\sqrt[4]{(\alpha_3 - \rho)^2 + \eta^2}$, $k_q^2 = \frac{1}{2} + 2\frac{\rho - \alpha_3}{p^2}$, $b = \sqrt{\alpha_3 - y}$, $y(z) = \delta^2(z)$, $c_\pm = \sqrt{2\left[\sqrt{(y-\rho)^2 + \eta^2} \pm (\rho - y)\right]}$, $M^2 = (2sb + c_+)^2 + c_-^2$, and $N^2 = (2sb - c_+)^2 + c_-^2$.

These functions and consequently, the whole family of solutions depend on three arbitrary real parameters α_3, ρ, η (22, 31). The periods in z and t also depend on these parameters. They are given by $\mathcal{Z} = 8K(k)/\mu$ and $\mathcal{T} = 4K(k_q)/p$, respectively, where $K(k)$ is the complete elliptic integral of the first kind.

Calculation of Theoretical Solutions. Theoretical solutions plotted in comparison with experimental results are particular solutions of Eq. **1** characterized by three arbitrary parameters α_1, α_2, and α_3. These parameters, which are nonzero roots of a fourth-order polynomial (31), are calculated by matching power and phase initial conditions between analytical zero- and first-order Fourier components and experimental three waves (pump, signal, and idler). In case of A-type solutions, α_1 and α_2 are complex, and so, two other parameters ρ and η are defined as $\alpha_1 = \alpha_2^* = \rho + i\eta$. The space–time evolution of theoretical solutions is then obtained by direct calculations from Eqs. **3**–**5**.

Optical Normalization. In order to apply the theory in the first section to optical fibers, the variables must be renormalized. To this end, the dimensional distance Z, time T (in the frame traveling at light group velocity), and field Ψ (with $|\Psi|^2$ giving directly the power in watts) are obtained by the following rescaling:

$$Z = (z - z_0)L_{NL}, \quad T = t\, T_s, \quad \Psi = \psi\sqrt{P_P}, \qquad [6]$$
$$L_{NL} = (\gamma P_P)^{-1}, \quad T_s = \sqrt{|\beta_2|L_{NL}}, \qquad [7]$$

where L_{NL} is the characteristic nonlinear length scale associated with CW power P_p and T_s is the relative temporal scale associated with dispersion. Here, z_0 is a suitable shift that accounts for the fact the input $Z = 0$ corresponds to a point of weak modulation in the solution (whereas $z = 0$ is the point of maximum amplification in the solution). For practical purposes, we can approximate $z_0 \approx \mathcal{Z}/4$, valid for weak-enough input modulation.

Water Wave Normalization. In order to introduce a normalization akin to Eqs. **6** and **7**, the dimensional distance along the tank Z, the dimensional time T, and the envelope of water wave elevation Ψ can be expressed in terms of nonlinear length L_{NL} and temporal scale T_s, fixed by the input envelope elevation a, as follows (also ref. 57):

$$Z = (z - z_0)\, L_{NL}, \quad T = t\, T_s, \quad \Psi = \psi\, a, \qquad [8]$$

where $L_{NL} = \frac{1}{\kappa^3 a^2}$, $T_s = \sqrt{\frac{2}{g\kappa^3 a^2}}$, and z_0 is a suitable shift for which considerations analogous to those made in optics are still valid. It is worth mentioning that in this case, the time T is also measured in the frame moving with the group velocity $c_g = \frac{\omega}{2\kappa}$. Obviously, this scaling is not unique. An equivalent choice often employed in the case of water waves can be written in terms of the wave number κ and the wave steepness $\varepsilon = a\kappa$: $Z = z/(\kappa\varepsilon^2)$, $T = \sqrt{2}t/(\omega\varepsilon)$, and $\Psi = \psi\varepsilon/\kappa$.

1. V. I. Bespalov, V. I. Talanov, Filamentary structure of light beams in nonlinear liquids. *Sov. Phys. JETP Lett.* **3**, 307 (1966).
2. T. B. Benjamin, J. Feir, The disintegration of wave trains on deep water part 1. theory. *J. Fluid Mech.* **27**, 417–430 (1967).
3. T. B. Benjamin, Instability of periodic wavetrains in nonlinear dispersive systems. *Proc. R. Soc. Lond. A* **299**, 59–76 (1967).
4. B. M. Lake, H. C. Yuen, H. Rungaldier, W. E. Ferguson, A note on some nonlinear water-wave experiments and the comparison of data with theory. *J. Fluid Mech.* **83**, 49–74 (1977).
5. H. C. Yuen, B. M. Lake, Nonlinear dynamics of deep-water gravity waves. *Adv. Appl. Mech.* **22**, 229 (1982).
6. M. P. Tulin, T. Waseda, Laboratory observations of wave group evolution, including breaking effects. *J. Fluid Mech.* **378**, 197–232 (1999).
7. O. Kimmoun *et al.*, Modulation instability and phase-shifted Fermi-Pasta-Ulam recurrence. *Sci. Rep.* **6**, 28516 (2016).
8. K. Tai, A. Hasegawa, A. Tomita, Observation of modulational instability in optical fibers. *Phys. Rev. Lett.* **56**, 135–138 (1986).
9. A. Mussot, A. Kudlinski, M. Droques, P. Szriftgiser, N. Akhmediev, Fermi-Pasta-Ulam recurrence in nonlinear fiber optics: The role of reversible and irreversible losses. *Phys. Rev. X* **4**, 011054 (2014).
10. A. Mussot *et al.*, Fibre multi-wave mixing combs reveal the broken symmetry of Fermi-Pasta-Ulam recurrence. *Nat. Photon.* **12**, 303–308 (2018).
11. D. Pierangeli *et al.*, Observation of Fermi-Pasta-Ulam-Tsingou recurrence and its exact dynamics. *Phys. Rev. X* **8**, 041017 (2018).
12. M. Remoissenet, *Waves Called Solitons: Concepts and Experiments* (Springer, 2013).
13. G. P. Agrawal, *Nonlinear Fiber Optics* (Academic Press, San Diego, CA, ed. 2, 1995).
14. C. C. Mei, *The Applied Dynamics of Ocean Surface Waves* (World Scientific, 1983), vol. 1.
15. A. Osborne, *Nonlinear Ocean Waves and the Inverse Scattering Transform* (Academic Press, 2010).
16. M. Daniel, S. Rajasekar, *Nonlinear Dynamics* (Narosa, 2009).
17. N. Akhmediev, V. I. Korneev, Modulation instability and periodic solutions of the nonlinear Schrödinger equation. *Theor. Math. Phys.* **69**, 1089–1093 (1986).
18. G. Van Simaeys, P. Emplit, M. Haelterman, Experimental demonstration of the Fermi-Pasta-Ulam recurrence in a modulationally unstable optical wave. *Phys. Rev. Lett.* **87**, 033902 (2001).
19. G. Van Simaeys, P. Emplit, M. Haelterman, Experimental study of the reversible behavior of modulational instability in optical fibers. *J. Opt. Soc. Am. B* **19**, 477–486 (2002).
20. E. Fermi, J. Pasta, S. Ulam, "Studies of nonlinear problems" in *Collected Papers of Enrico Fermi* (The University of Chicago Press, 1965), vol. 2, pp. 977–988.
21. N. Akhmediev, D. Heatley, G. Stegeman, E. Wright, Pseudo-recurrence in two-dimensional modulation instability with a saturable self-focusing nonlinearity. *Phys. Rev. Lett.* **65**, 1423–1426 (1990).
22. M. Conforti, A. Mussot, A. Kudlinski, S. Trillo, N. Akhmediev, Doubly periodic solutions of the focusing nonlinear Schrödinger equation: Recurrence, period doubling, and amplification outside the conventional modulation-instability band. *Phys. Rev.* **101**, 023843 (2020).
23. L. N. Trefethen, A. E. Trefethen, S. C. Reddy, T. A. Driscoll, Hydrodynamic stability without eigenvalues. *Science* **261**, 578–584 (1993).
24. C. Mahnke, F. Mitschke, Possibility of an Akhmediev breather decaying into solitons. *Phys. Rev. A* **85**, 033808 (2012).
25. N. V. Priya, M. Senthilvelan, M. Lakshmanan, Akhmediev breathers, Ma solitons, and general breathers from rogue waves: A case study in the Manakov system. *Phys. Rev. E* **88**, 022918 (2013).
26. B. Varlot, Y. Chembo, C. Finot, Akhmediev breathers as ultra-wideband pulses. *Microw. Opt. Technol. Lett.* **56**, 664 (2014).
27. K. Hammani *et al.*, Spectral dynamics of modulation instability described using Akhmediev breather theory. *Optic Lett.* **36**, 2140–2142 (2011).
28. A. Bendahmane *et al.*, Optimal frequency conversion in the nonlinear stage of modulation instability. *Opt. Express* **23**, 30861–30871 (2015).
29. G. Yang, F. O. Wu, H. E. L. Aviles, D. Christodoulides, Optical amplification and transmission of attenuated multi-soliton based on spectral characteristics of Akhmediev breather. *Opt. Commun.* **473**, 125899 (2020).
30. U. Andral, B. Kibler, J. M. Dudley, C. Finot, Akhmediev breather signatures from dispersive propagation of a periodically phase-modulated continuous. *Wave Motion* **95**, 102545 (2020).
31. N. Akhmediev, V. M. Eleonskii, N. E. Kulagin, Exact solutions of the first order of nonlinear Schrödinger equation. *Theor. Math. Phys.* **72**, 809–818 (1987).
32. N. Akhmediev, A. Ankiewicz, First-order exact solutions of the nonlinear Schrödinger equation in the normal-dispersion regime. *Phys. Rev. A* **47**, 3213–3221 (1993).
33. D. Mihalache, F. Lederer, D. M. Baboiu, Two-parameter family of exact solutions of the nonlinear Schrödinger equation describing optical-soliton propagation. *Phys. Rev. A* **47**, 3285–3290 (1993).
34. D. Mihalache, N. C. Panoiu, Analytic method for solving the nonlinear Schrodinger equation describing pulse propagation in dispersive optic fibres. *J. Phys. Math. Gen.* **26**, 2679–2697 (1993).
35. L. Gagnon, Solitons on a continuous-wave background and collision between two dark pulses: Some analytical results. *J. Opt. Soc. Am. B* **10**, 469–474 (1993).
36. J. M. Dudley, G. Genty, A. Mussot, A. Chabchoub, F. Dias, Rogue waves and analogies in optics and oceanography. *Nat. Rev. Phys.* **1**, 675–689 (2019).
37. M. Onorato, S. Residori, U. Bortolozzo, A. Montina, F. T. Arecchi, Rogue waves and their generating mechanisms in different physical contexts. *Phys. Rep.* **528**, 47–89 (2013).
38. S. Chen, F. Baronio, J. M. Soto-Crespo, P. Grelu, D. Mihalache, Versatile rogue waves in scalar, vector, and multidimensional nonlinear systems. *J. Phys. Math. Theor.* **50**, 463001 (2017).
39. B. Ghosh, S. Banerjee, Modulation instability of ion-acoustic waves in plasma with nonthermal electrons. *J. Astrophys.* **2014**, 785670 (2014).
40. X. X. Li, R. J. Cheng, A. X. Zhang, J. K. Xue, Modulational instability of Bose-Einstein condensates with helicoidal spin-orbit coupling. *Phys. Rev.* **100**, 032220 (2019).
41. J. Ye, S. T. Cundiff, *Femtosecond Optical Frequency Comb Technology: Principle, Operation, and Application* (Kluver Academic Publishers, 2005).
42. E. J. Greer, D. M. Patrick, P. G. J. Wigley, J. R. Taylor, Generation of 2 THz repetition rate pulse trains through induced modulational instability. *Electron. Lett.* **25**, 1246–1248 (1989).
43. J. M. Dudley, J. R. Taylor, *Supercontinuum Generation in Optical Fibers* (Cambridge University Press, 2010).
44. C. Kharif, E. Pelinovsky, A. Slunyaev, *Rogue Waves in the Ocean* (Springer, 2009).
45. S. Trillo, S. Wabnitz, Dynamics of the nonlinear modulational instability in optical fibers. *Opt. Lett.* **16**, 986–988 (1991).
46. G. Vanderhaegen *et al.*, Observation of doubly periodic solutions of the nonlinear Schrödinger equation in optical fibers. *Opt. Lett.* **45**, 3757–3760 (2020).
47. C. Naveau *et al.*, Full-field characterization of breather dynamics over the whole length of an optical fiber. *Opt. Lett.* **44**, 763–766 (2019).
48. K. B. Dysthe, Note on a modification to the nonlinear Schrödinger equation for application to deep water waves. *Proc. R. Soc. Lond. A Math. Phys. Sci.* **369**, 105–114 (1979).
49. T. Waseda, W. Fujimoto, A. Chabchoub, On the asymmetric spectral broadening of a hydrodynamic modulated wave train in the optical regime. *Fluids* **4**, 84 (2019).
50. N. R. Newbury, Searching for applications with a fine-tooth comb. *Nat. Photon.* **5**, 186–188 (2011).
51. D. ter Haar, V. N. Tsytovich, Modulation instabilities in astrophysics. *Phys. Rep.* **73**, 175–236 (1981).
52. Y. H. Ichikawa, T. Suzuki, T. Taniuti, Modulation instability of electron plasma wave. *J. Phys. Soc. Jpn.* **34**, 1089–1092 (1973).
53. S. G. Thornhill, D. Ter Haar, Langmuir turbulence and modulational instability. *Phys. Rep.* **43**, 43–99 (1978).
54. G. Xu, J. McNiff, A. Boardman, B. Kibler, Space-time evolution of optical breathers and modulation instability patterns in metamaterial waveguides. *Wave Motion* **93**, 102448 (2020).
55. J. H. V. Nguyen, D. Luo, R. G. Hulet, Formation of matter-wave soliton trains by modulational instability. *Science* **356**, 422–426 (2017).
56. P. J. Everitt *et al.*, Observation of a modulational instability in Bose-Einstein condensates. *Phys. Rev. A* **96**, 041601 (2017).
57. R. El Koussaifi *et al.*, Spontaneous emergence of rogue waves in partially coherent waves: A quantitative experimental comparison between hydrodynamics and optics. *Phys. Rev. E* **97**, 012208 (2018).

PHYSICS

Vanderhaegen et al.
"Extraordinary" modulation instability in optics and hydrodynamics

PNAS | 7 of 7
https://doi.org/10.1073/pnas.2019348118